Laboratory implementation of quantum-control-mechanism identification through Hamiltonian encoding and observable decoding

R. Rey-de-Castro and H. Rabitz
Department of Chemistry, Princeton University, Princeton, New Jersey 08544, USA
(Received 16 February 2010; published 28 June 2010)

We report on the laboratory implementation of quantum-control-mechanism identification through Hamiltonian encoding and observable decoding (HE-OD). Over a sequence of experiments, HE-OD introduces a special encoded signature into the components of a previously determined control field expressed in a chosen representation. The outcome appears as a modulated signal in the controlled system observable. Decoding the modulated signal identifies the hierarchy of correlations between components of the control field in a particular representation. In cases where the initial quantum state and observable operator are fully known, then HE-OD can also identify the transition amplitudes of the various Dyson expansion orders contributing to the controlled dynamics. The basic principles of HE-OD are illustrated for second harmonic generation when the components of the field representation are simply taken as the pixels in the pulse shaper. The outcome of HE-OD agrees well with simulations, verifying the concept.

DOI: 10.1103/PhysRevA.81.063422 PACS number(s): 32.80.Qk, 42.62.Fi, 42.50.Ct, 42.50.Dv

I. INTRODUCTION

The control of quantum dynamics phenomena is receiving increasing attention, and a practical paradigm is closed-loop learning control which optimizes an output signal through an algorithmically guided adaptation of the system controls [1]. Closed-loop-based quantum control has been successfully achieved in a growing variety of applications [2] including selective molecular dissociation [3], discrimination of almost identical molecules [4], selective multiphoton ionization [5], tailored x-ray generation [6], control of lattice vibrations [7], spatio-temporal control of nanostructures [8], and even the control of the shape of a wave function [9]. The detailed structure of the associated optimal control fields is often non-intuitive, especially for systems driven in a highly nonlinear fashion and for those with complex dynamics. Thus, a physical interpretation of optimal control fields is a challenging task. Furthermore, there will typically be multiple sets of controls producing the same outcome [4]. This situation implies that different mechanisms can give rise to the same output yield. At this stage of development in controlling quantum dynamics, the notion of mechanism is still subject to definition. An important goal is to learn as much as possible about control mechanism directly from appropriate experiments without resorting to dynamical simulations, which are difficult to reliably perform in complex systems. In order to address the latter challenges, a laboratory-implementable technique referred to as mechanism identification through Hamiltonian encoding and observable decoding (HE-OD) has been proposed [10–14]. HE-OD deduces mechanistic information by encoding the Hamiltonian through a sequence of specifically designed perturbations to the control and decoding the resultant system response. The mechanism is then obtained in the form of correlations among the control variables, which can be further analyzed to yield pathway amplitudes in the Dyson expansion of the evolution operator [13].

In contrast to HE-OD, other methods to extract mechanistic information generally seek to perform modeling using the observed control field, possibly along with additional supporting experimentation. For example, mechanistic information has been obtained from numerical simulations aided by pump-probe experiments [15–17]. Characterization of the optimum field along with previous knowledge about the system has been used to guide modeling [18,19]. The complexity of the problem may be reduced in some circumstances by identifying an important subset of control variables, and in favorable cases this can lead to obtaining a new control field basis better suited to the problem at hand [20–24]. In some situations it is possible to restrict the learning algorithm to search over a subset of fields whose action on the system is already physically understood [25]. The full set of control fields deduced by the learning algorithm in every iteration toward optimization has been subjected to statistical correlation analyses to obtain mechanistic information [26,27]. All of these methods address particular aspects of control mechanism assessment, and they may be viewed as providing information complementary to that extracted from HE-OD.

Ideally, mechanistic information could be determined in real time during feedback-control experiments. The additional information for the learning algorithm could be used to redirect the controls toward achieving a desired dynamical goal while also steering the system along a favorable mechanistic path. Such a real-time procedure would only be possible when the method for identifying the mechanism does not require computationally intensive modeling of the system dynamics. HE-OD has the capability of real-time laboratory operation, which will be demonstrated in a follow-up work. The present paper aims to present the basic principles of HE-OD and provide a simple laboratory implementation to verify these principles.

The paper is organized as follows. In Sec. II HE-OD is expressed in a general fashion including for cases when little *a priori* information is known about the system. Section III specifies the field representation used in this work as well as the particular encoding procedure employed in the experiments. In Sec. IV HE-OD is applied to the simple case of second harmonic generation (SHG). This initial test case was chosen for its well-documented behavior [28], which permits easy testing of HE-OD by comparing the expected results to the experimental findings. Importantly, HE-OD is a generic mechanism analysis tool and the simple illustration here

shows the basic elements which may now be implemented in more complex systems. The laboratory setup is also discussed in Sec. IV as well as the results of the experimental implementation of HE-OD. Section V presents a mechanism analysis from the experimental results of Sec. IV and compares this with simulations. Concluding remarks are given in Sec. VI.

II. PRINCIPLES OF HE-OD

The HE-OD technique is set forth here for a quantum system under manipulation by an optical electric field $E(t)$. The system Hamiltonian is considered to have the form $H = H_0 - \mu E(t)$, where H_0 is the unperturbed Hamiltonian and μ is the dipole moment operator. The HE-OD technique can be applied in the laboratory without knowledge of H_0 and μ. Additionally, the Hamiltonian could even have an unknown form, as HE-OD is a means for directly identifying the relationship between the input control field structure and the output dynamical response. However, knowledge of the form of the Hamiltonian [e.g., $H = H_0 - \mu E(t)$] greatly aids in interpreting the input–output relationship revealed by HE-OD. In this section we adopt the dipole coupling form for clarity of illustration.

The system dynamics is governed by the evolution operator $U(t)$ satisfying the time-dependent Schrödinger equation in the interaction representation,

$$i\hbar \frac{dU(t)}{dt} = \mu_I(t)E(t)U(t), \tag{1}$$

with $\mu_I(t) = -\exp(-\frac{i}{\hbar}H_0 t)\mu \exp(\frac{i}{\hbar}H_0 t)$ and $U(0) = I$. The basic HE-OD concepts are presented here in the context of a closed quantum system undergoing unitary dynamics. An extended formulation also could be considered for open systems with nonunitary dynamics. The laboratory implementation of HE-OD is the same in both cases, but the analysis and interpretation of the results depend on the particular circumstances. The solution of Eq. (1) can be expressed in terms of the Dyson expansion

$$U(T) = I + \sum_{n=1}^{\infty} \left(\frac{1}{i\hbar}\right)^n U^{(n)}(T), \tag{2}$$

where

$$U^{(n)}(T) = \int_0^T \int_0^{t_n} \int_0^{t_{n-1}} \cdots \int_0^{t_2} \mu_I(t_n)E(t_n)\mu_I(t_{n-1})E(t_{n-1}) \times \cdots \mu_I(t_1)E(t_1)\, dt_1 \cdots dt_{n-1}dt_n, \tag{3}$$

with the index n referring to the order [i.e., the power of $E(t)$ in the particular term] of $U^{(n)}$. Here T is the target time for performing an observation, but it could also be considered as a variable labeling a sequence of temporal observations. The convergence of the Dyson expansion for realistic pulses of finite energy was proved in Ref. [10]. The ultimate goal of HE-OD is to identify the significant contributing terms $U^{(n)}$, $n = 1,2,\ldots$, directly from laboratory data. To proceed further a practical representation needs to be chosen for the field $E(t)$. The following general expression is useful for illustrating the basic field encoding concept:

$$E(t) = \sum_{p=-\sigma}^{\sigma} a_p \epsilon_p(t). \tag{4}$$

The number of expansion functions is $2\sigma + 1$, and the set $\{\epsilon_p(t)\}$ is assumed to be appropriately chosen for the particular intended application. Since the field $E(t)$ is real, if the basis functions $\epsilon_p(t)$ are taken as complex, then it may be convenient to choose $\epsilon_{-p}(t) = \epsilon_p^*(t)$. The most common example is the Fourier representation with spectral components $\epsilon_p(t) = e^{i\omega_p t}$, which is a natural basis for pulse-shaping experiments where the expansion coefficients $a_p = |a_p|e^{i\phi_p}$ can be directly set by controlling the shaper amplitudes $|a_p|$ and phases ϕ_p, with $|a_{-p}| = |a_p|$ and $\phi_{-p} = -\phi_p$. Virtually any other field representation may be utilized with HE-OD, as dictated by the physics of the problem, including expansions in terms of Gaussian or polynomial-phase functions, time-frequency functions, etc. [23,29,30]. Notwithstanding the freedom in choosing the representation of the field, the mechanistic insight obtained by HE-OD will be in reference to the particular field form. Thus, distinct physical insights about the mechanism could arise from the same field $E(t)$, according to how it is represented for a HE-OD analysis.

The quantum system evolution following Eq. (1) results in a nonlinear mixing of field components, as evident in Eq. (3). Substituting Eq. (4) into Eq. (3) yields

$$U^{(n)}(T) = \sum_{p_n} \sum_{p_{n-1}} \cdots \sum_{p_1} \left(\frac{1}{i\hbar}\right)^n U^{n(p_1 \cdots p_n)}(T) \tag{5}$$

and

$$U(T) = I + \sum_{n=1}^{\infty} \left(\sum_{p_n} \sum_{p_{n-1}} \cdots \sum_{p_1} \left(\frac{1}{i\hbar}\right)^n U^{n(p_1 \cdots p_n)}(T) \right) \tag{6}$$

with

$$U^{n(p_1 \cdots p_n)}(T) = \int_0^T \int_0^{t_n} \cdots \int_0^{t_2} \times \mu_I(t_n)a_{p_n}\epsilon_{p_n}(t_n)\mu_I(t_{n-1})a_{p_{n-1}}\epsilon_{p_{n-1}}(t_{n-1}) \times \cdots \mu_I(t_1)a_{p_1}\epsilon_{p_1}(t_1)dt_1 \cdots dt_{n-1}dt_n, \tag{7}$$

The collection of physically relevant matrix elements of $U^{n(p_1 \cdots p_n)}(T)$,$n = 1,2,\ldots$, of significant magnitude for the system observable specifies the control mechanism in the context of HE-OD.

The first step in HE-OD is to encode the field as follows. Consider a sequence of experiments labeled by an index $k = 1,2,\ldots$ with the control field in the kth experiment $E(t,s_k)$ now labeled by the variable s_k and given by

$$E(t,s_k) = \sum_{p=-\sigma}^{\sigma} a_p h_p(s_k)\epsilon_p(t). \tag{8}$$

Here $h_p(s_k)$ is a time-independent encoding function which depends on the variable s_k,$k = 1,2,\ldots$. As will be shown in the following, it is desirable to choose the encoding functions $h_p(s_k)$ with some specific properties to facilitate the extraction of mechanistic information from dynamical observations. In practice some of the functions $h_p(s_k)$ may be set to 1 to

selectively encode the remaining portion of the field to deduce its particular role in the controlled dynamics. Substituting the encoded field of Eq. (8) in place of the original field of Eq. (4) into the terms of Eq. (6) results in the modulated evolution operator

$$U(T,s_k) = I + \sum_{n=1}^{\infty}\left(\sum_{p_n}\sum_{p_{n-1}}\cdots\sum_{p_1} h_{p_n}(s_k)h_{p_{n-1}}(s_k)\cdots h_{p_1}(s_k) \times \left(\frac{1}{i\hbar}\right)^n U^{n(p_1\cdots p_n)}(T)\right). \quad (9)$$

Each term $U^{n(p_1\cdots p_n)}(T)$ in the expansion of the evolution operator is now modulated by an associated product of encoding functions $h_{p_n}(s_k)h_{p_{n-1}}(s_k)\cdots h_{p_1}(s_k)$.

The expectation value of an observable operator $\mathscr{O}$ is given by

$$\langle\mathscr{O}(T)\rangle = \mathrm{Tr}[\rho\mathscr{O}] = \mathrm{Tr}[U(T)\rho(0)U^{\dagger}(T)\mathscr{O}], \quad (10)$$

where $\rho(0)$ is the initial density matrix. In Eq. (10) the observable operator $\mathscr{O}$ is considered as time independent, but that could be relaxed if appropriate. In addition, as remarked earlier, T could be a running variable for temporal observations. Upon encoding the field in Eq. (8), the observable expectation value in Eq. (10) becomes modulated,

$$\langle\mathscr{O}(T,s_k)\rangle = \mathrm{Tr}[U(T,s_k)\rho(0)U^{\dagger}(T,s_k)\mathscr{O}]. \quad (11)$$

The *set* of observable modulating functions is defined as the collection of all possible products of the encoding functions $h_p(s_k)$. In practice, it is not necessary to consider "all possible" products, as the series in Eq. (9) will converge to some acceptable tolerance (e.g., dictated by the laboratory observable noise level) at a finite order n. If the relevant set of modulating functions forms an orthogonal basis set, then the measured modulated data $\langle\mathscr{O}(t,s_k)\rangle, k = 1,2,\ldots,$ can be decoded by projecting them onto the members of the basis set. This attractive orthogonality property leads to some practical choices for encoding functions, as shown in the following. It is also possible to use a nonorthogonal basis set, but then the decoding process becomes more complex, calling for special attention to data noise and associated instabilities in extracting the desired mechanistic coefficients. Hereafter, we will assume that the encoding functions form an orthonormal product set. A decoded projection of order m is defined as

$$P(j_1,\ldots,j_m) = \frac{1}{N}\sum_{k=1}^{N}\langle\mathscr{O}(T,s_k)\rangle F^*(j_1,\ldots,j_m;s_k), \quad \forall j_k,k, \quad (12)$$

where N is the number of experiments, and the corresponding modulating function is given by

$$F(j_1,\ldots,j_m;s_k) = h_{j_1}(s_k)h_{j_2}(s_k)\cdots h_{j_m}(s_k). \quad (13)$$

Equations (9), (11), and (12) show that the projection $P(j_1,\ldots,j_m)$ is bilinear in the matrix elements of $U(T)$ and linear in a product of appropriate matrix elements of $\rho(0)$ and $\mathscr{O}$. If the matrix elements of $\rho(0)$ and $\mathscr{O}$ are known, then it is possible to obtain the matrix elements of $U^{m(j_1\cdots j_m)}(t)$ from the system of equations (12). A procedure for solving these equations in the case where $\rho(0)$ and $\mathscr{O}$ correspond to making a pure-state transition is given in Ref. [14], and the logic may be extended to mixed states and more general observables.

If neither $\rho(0)$ nor $\mathscr{O}$ is fully known, it is still possible to obtain valuable information from the extracted projections $P(j_1,\ldots,j_m)$. As shown in the following, the latter projections, readily decoded from $\langle\mathscr{O}(T,s_k)\rangle$, provide mechanistic insights by revealing the set of nonlinear correlations among the control field variables contributing to the observable. The extraction of the projections $P(j_1,j_2,\ldots,j_m)$ is the first data analysis step with HE-OD, and in some cases this view of mechanism may suffice. HE-OD can be adapted to the nature of the information, both known *a priori* and desired, from the controlled system dynamics by designing a particular encoding scheme consistent with these circumstances. When little is known about the system dynamics, reducing the encoding to a small portion of the control field variables makes it possible to simplify the decoding. To see this, consider the scenario where most of the field components are not encoded, or, equivalently, where most of the encoding functions in Eq. (8) are fixed at $h_p(s_k) = 1$, $\forall s_k$, and just a small set of m' functions (i.e., $m' \ll 2\sigma + 1$) actually vary with respect to s_k. With this choice, the modulated evolution operator is now given by

$$\begin{aligned} U(T,s_k) &= U_0(T) + \sum_{n=1}^{\infty}\left(\sum_{p_n}\sum_{p_{n-1}}\cdots\sum_{p_1} h_{p_n}(s_k)h_{p_{n-1}}(s_k) \times\cdots h_{p_1}(s_k)\left(\frac{1}{i\hbar}\right)^n U^{n(p_1\cdots p_n)}(T)\right) \\ &= U_0(T) + U^{\mathrm{mod}}(T,s_k), \end{aligned} \quad (14)$$

where $U_0(T)$ is the sum of all *totally* nonmodulated terms of the evolution operator expansion, and $U^{\mathrm{mod}}(T,s_k)$ has a dependence on s_k through the varying encoding functions. Since the encoding is minimal, $U_0(T)$ is approximately equal to $U(T)$ and a reasonable expectation is that $||U_0(T)|| \approx 1 \gg ||U^{\mathrm{mod}}(T,s_k)||$. Introducing Eq. (14) into Eq. (11) results in

$$\begin{aligned} \langle\mathscr{O}(T,s_k)\rangle &= \mathrm{Tr}\{[U_0(T) + U^{\mathrm{mod}}(T,s_k)]\rho(0)[U_0(T) + U^{\mathrm{mod}}(T,s_k)]^{\dagger}\mathscr{O}\} \\ &\approx \mathrm{Tr}[U_0(T)\rho(0)U_0^{\dagger}(T)\mathscr{O}] + \sum_{n}^{\infty}\sum_{p_n\ldots p_1} h_{p_n}(s_k)\cdots h_{p_1}(s_k) \times \mathrm{Tr}[U_0(T)\rho(0)U^{n(p_1\ldots p_n)\,\dagger}(T)\mathscr{O}] + \mathrm{c.c.}, \end{aligned} \quad (15)$$

where only terms first order in $U^{\mathrm{mod}}(T,s_k)$ are retained. Projections of the observed data now give

$$P(j_1,\ldots,j_m) \approx \mathrm{Tr}[U_0(T)\rho(0)U^{m(j_1\cdots j_m)\,\dagger}(T)\mathscr{O}], \quad \forall j_i,m. \quad (16)$$

The extracted projections $P(j_1,\ldots,j_m)$ are bilinear in the underlying dynamics through their dependence on $U_0(T)$ and $U^{n(p_1\ldots p_n)\,\dagger}(T)$. However, the extraction of the latter amplitudes poses a far easier problem than the general case of Eqs. (11) and (12). Moreover, the magnitude of the projection $P(j_1,\ldots,j_m)$ is proportional to $||U^{m(j_1\ldots j_m)}(T)||$. As a result,

$|P(j_1,\ldots,j_m)|$ gives an estimate of the contribution to the observable $\langle\mathcal{O}\rangle$ of the nonlinear process that mixes field components as $[\epsilon(t)]^{j_1}\times[\epsilon(t)]^{j_2}\times\cdots\times[\epsilon_m(t)]^{j_m}$. Knowledge of the field nonlinearities present in the observable can be of direct use for mechanistic purposes. This feature of HE-OD is illustrated later in the paper.

III. PRACTICAL LABORATORY ENCODING

In principle, virtually any set of functions $h_p(s_k)$ could be chosen to encode the field, provided that their products in Eq. (16) form a linearly independent set, up to the highest significant order encountered in the Dyson expansion. The experiments in this work employ

$$h_p(s_k)=\exp[if_p(s_k)], \tag{17}$$

where $f_p(s_k)$ is a random function with a uniform distribution in the interval $[0,2\pi]$. This set of encoding functions $h_p(s_k)$ follows useful associative and orthogonality requirements. The product of two random-phase functions $h_p(s_k)$ and $h_q(s_k)$ is another random-phase function $h_r(s_k)$ with the same properties:

$$\begin{aligned}h_p(s_k)\times h_q(s_k)&=e^{if_p(s_k)}e^{if_q(s_k)}\\&=e^{i[f_p(s_k)+f_q(s_k)]}=e^{if_r(s_k)}\\&=h_r(s_k).\end{aligned} \tag{18}$$

Here it is understood that $f_r(s_k)=f_p(s_k)+f_q(s_k)$ is taken as $\mathrm{mod}(2\pi)$. Thus, the product of any number of encoding functions also belongs to the same function set. The latter property is important, as the modulating function of order m in Eq. (13) will involve the product of m encoding functions. By defining the scalar product of two functions $h_p(s_k)$ and $h_q(s_k)$, with $k=1,2,\ldots,N$, as

$$h_p\circ h_q=\frac{1}{N}\sum_{k=1}^{N}h_p(s_k)h_q^*(s_k), \tag{19}$$

one can see that the random-phase function set is approximately orthonormal,

$$\begin{aligned}h_p(s_k)\circ h_q(s_k)&=\frac{1}{N}\sum_{k=1}^{N}h_p(s_k)h_q^*(s_k)\\&=\frac{1}{N}\sum_{k=1}^{N}e^{i[f_p(s_k)-f_q(s_k)]}\\&\simeq\delta_{pq}.\end{aligned} \tag{20}$$

Establishing the value of N in Eqs. (12) and (19) is important for the practical execution of HE-OD. The scalar products in those equations are best viewed as integrals over the continuous encoding index s, with Monte Carlo random sampling $s_k, k=1,2,\ldots$, used to approximate the integrals. Therefore, a large value of N is likely needed for good convergence of the projection operation. The demonstration experiment in this paper considers two variables where each one corresponds to a specific grouping of phase mask pixels subjected to modulation. Note that different few-variable modulations can be combined together, since the mechanism assessment can be approached in a hierarchical fashion with multiple small groupings of encoded controls. Taking five-bit resolution per variable in the present work gives a total of $32\times32=1024$ distinct laboratory samples $\langle\mathcal{O}(T,s_k)\rangle$. In the experiments described in the following, all these data points were first measured and stored in a database. Then, the projections were formed from a sample size of $N=200{,}000$ randomly drawn data points from the database along with the exact values of the associated modulation functions $F(j_1,j_2;s_k)$. As the number m of encoding basis functions rises, the orthogonality demand of Eq. (20) may call for additional sampling when forming the database.

IV. HE-OD DEMONSTRATION EXPERIMENT

This paper presents a proof-of-principle experiment applying HE-OD to SHG as a simple test system. The well-established physical basis of this system permits accurate modeling to assess the experimental results (see Sec. V).

A. Experimental setup

The experiment used a Ti:sapphire femtosecond laser, consisting of a Spectra-Physics Tsunami oscillator and a 1-kHz, 1.8-mJ Spitfire amplifier. The amplified pulses had a full width at half maximum (FWHM) of 12.4 nm centered at 796 nm, which corresponds to pulses of duration ~100 fs FWHM. Phase modulation was performed with a 4-f configuration pulse shaper having a liquid-crystal display (LCD) with 128 liquid-crystal pixels (SLM-256, CRI). When the laser pulse spectrum is spread on the LCD (see Fig. 1) there is a linear relationship between optical frequency and position on the LCD; a 0.22-nm portion of the infrared (IR) bandwidth passed through each of the 128 pixels. In the remainder of the paper, optical frequency is referred to in units of LCD pixels.

The amplitude of the input IR electric field $|E(\omega)|$ was determined (within a proportionality constant) by taking the square root of the measured spectrum. The phase of the electric field was obtained by first finding the SLM phase mask that optimizes the SHG signal which was set as a reference. The phase corresponding to any given SLM mask is just its difference from the reference phase based upon calibration of the pulse shaper.

The second harmonic light was produced by focusing the shaped pulse onto a 100-nm-thick type-I BaB_2O_4 (BBO) crystal. The laser intensity at the BBO crystal was $\sim2.5\times10^{11}$ W/cm^2 for a transform-limited pulse, well within the non-depleted low-power regime. The SHG spectrum was recorded with an Ocean Optics HR-2000 400-nm spectrometer. The signal was the integral over a 0.3-nm window of the SHG spectrum centered around 398.3 nm. A diagram of the HE-OD system is shown in Fig. 1. The setup is similar to those commonly used in closed-loop quantum control [1]. Here the setup is used not as a loop to optimize the controls, but rather to experimentally implement the encoding-decoding HE-OD operations. This configuration is important, as HE-OD can be implemented using a standard learning control apparatus additionally guided by suitable software to perform the extra encoding of the control field and the subsequent decoding of the observable signal.

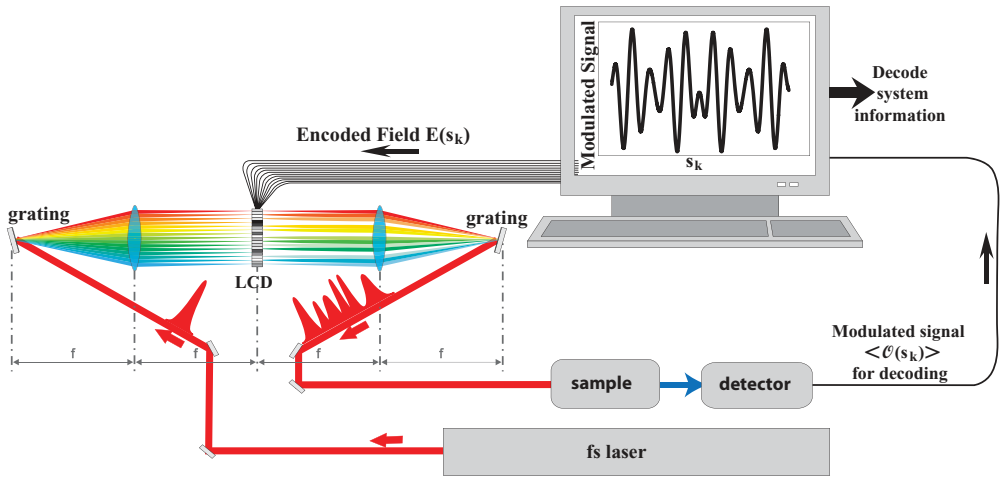

FIG. 1. (Color online) Setup for the HE-OD modulation experiments. The closed loop in this context is for performing encoding of the control field to extract mechanistic information. The HE-OD loop may be embedded within a learning loop using the same apparatus with the computer software swinging from guiding the search for an effective control to mechanism extraction and back again, etc. On-the-fly extracted mechanistic information could also be used to redirect the learning process toward seeking a control that meets the physical objective in balance with mechanistic guidance. The SHG demonstration experiment in this paper executed one cycle of this combined process.

B. Encoding SHG

In SHG two photons with frequencies ω_1 and ω_2 combine to produce another photon with frequency $\Omega = \omega_1 + \omega_2$. As the input laser pulse is spread over a frequency window, the electric field generated at frequency Ω is given by [28]

$$E_{\mathrm{SHG}}(\Omega) \propto |E(t)|^2 \propto \int_{-\infty}^{-\infty} E(\omega)E(\Omega-\omega)\,d\omega, \quad (21)$$

where $E(\omega)$ is the input electric field at frequency ω. The observed SHG signal is proportional to the square modulus of the generated electric field integrated over a recorded frequency band $\Delta\Omega$:

$$S_{\mathrm{SHG}} \propto \int_{\Delta\Omega} |E_{\mathrm{SHG}}(\Omega)|^2\,d\Omega. \quad (22)$$

Equation (21) can be interpreted as a sum of products of paired electric field amplitudes whose corresponding frequencies are symmetrical relative to $\Omega/2$. This situation is illustrated in Fig. 2, where the field pixel components of selected pairs are connected by arrows for a frequency $\Omega/2$ which is slightly shifted by $\zeta = \Omega/2 - \omega_0$ from the center of the input pulse spectrum located at ω_0. The figure shows two groups of encoded electric field components of width $\Delta = 5$ symmetrically located relative to the center of the spectrum at $\Omega/2$ (blue grouped pixels in Fig. 2.) The encoding of the latter two groups of pixels is done by multiplying one group of spectral components by $h_1(s_k) = \exp[if_1(s_k)]$ and the other group by $h_2(s_k) = \exp[if_2(s_k)]$. This encoding is easily implemented by setting the SLM to add a phase equal to $f_1(s_k)$ or $f_2(s_k)$ to the corresponding group of pixels. The remaining spectral components (yellow pixels in Fig. 2) are not encoded. To summarize, the encoding can be expressed as a piecewise function

$$E^{\mathrm{enc}}(\omega,s_k) = \begin{cases} E(\omega) \times e^{if_1(s_k)}, & \omega-\omega_0 \in [-\omega_c-\Delta/2, -\omega_c+\Delta/2], \\ E(\omega) \times e^{if_2(s_k)}, & \omega-\omega_0 \in [\omega_c-\Delta/2, \omega_c+\Delta/2], \\ E(\omega), & \text{otherwise.} \end{cases} \quad (23)$$

The experimental implementation of the encoding resulted in the random SHG signal shown in Fig. 3. Since there are two encoding functions $h_1(s_k)$ and $h_2(s_k)$, the projections $P(j_1,\ldots,j_m)$ defined in Eq. (12) only have two indices (j_1, j_2). The decoded projections from the data are shown in Fig. 4 and will be analyzed in Sec. V.

There can be significant cross-talk between pixels in a SLM due to voltage leaking [31] and/or diffraction effects [32] as near-infrared light goes through the ~100-μm-wide pixels. The cross-talk between pixels results in a smoothing of the transition between the phase and/or amplitude values of contiguous pixels. The real phase and/or amplitude mask is then the sum of a mask with sudden transitions (as an ideal SLM would produce) and small-bandwith components that smooth the transitions between pixels. These small-bandwidth components lead to the creation of long (~1 ns) pulses [31] that may have complex effects on the system dynamics. Cross-talk effects are further exacerbated by large phase changes

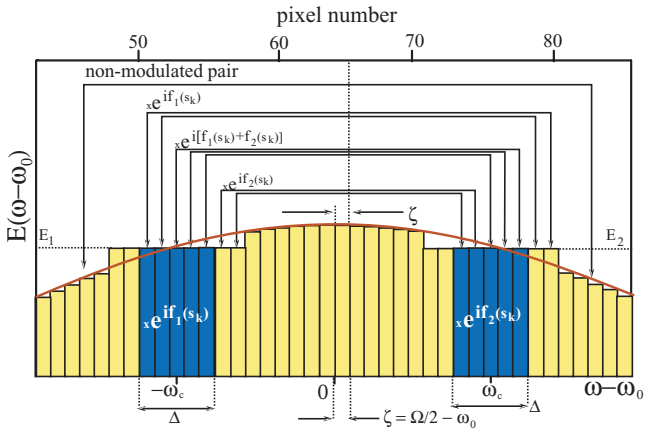

FIG. 2. (Color) Spectral dependence of the input pulse's electric field amplitude (solid red curve). The yellow and blue rectangles symbolize spectral components. The two groups of blue spectral components of width $\Delta = 5$ (measured in pixel units as explained in Sec. IV A) on the right and left are encoded by $e^{if_1(s_k)}$ and $e^{if_2(s_k)}$, respectively. The yellow spectral components are not encoded. The figure shows only part of the spectrum for clarity, and a large number of pixels are actually involved in the experiments. The arrows connect spectral components symmetrical to $\omega = \omega_0 + \zeta$ (where ω_0 corresponds to the center of the input field spectrum). When the spectral components of a pair are multiplied together in a SHG process the product has a modulation that depends on the position of the pair. Notice that some blue (encoded) pixels multiply yellow (unencoded) ones; this gives rise to first-order projections (when blue multiplies yellow) and second-order projections (when blue multiplies blue). The specific function that modulates some of the pairs is indicated over the arrow connecting a particular pair. The top abscissa scale gives the corresponding position of the spectral components on the LCD used in the experiments. The amplitude of each spectral component in general coincides with the solid curve, but the amplitudes of spectral components in and around the encoded regions are kept constant to illustrate the approximation to the field amplitudes utilized in the qualitative assessment of the SHG mechanism given in Sec. V.

between neighboring SLM pixels. Consideration of these issues suggests the use of smooth component functions in Eq. (4) to represent the controls with each function transcending many pixels. Nevertheless, the present work adopted a pixel basis to clearly illustrate the principles of HE-OD. The SLM used here only accepted phase changes in the $[0,2\pi]$ interval. Any phase whose value lies outside of this interval has to be wrapped around back to the $[0,2\pi]$ interval, and large phase discontinuities can appear at wrap-around points producing larger cross-talk effects. Given these issues, the random-phase functions were chosen here in order to confine the phase of each pixel to the interval $[0,2\pi]$, avoiding the need to wrap around and reducing cross-talk effects.

There is a maximum resolvable projection order analogous to the Nyquist frequency for discrete Fourier transforms. This fact is used here to estimate the projection error. The projections have errors originating not only from experimental noise but also from the numerical processing due to the approximate orthogonality of the modulating function set. As mentioned in Sec. III we used five-bit phase resolution. This resolution ultimately determines the maximum

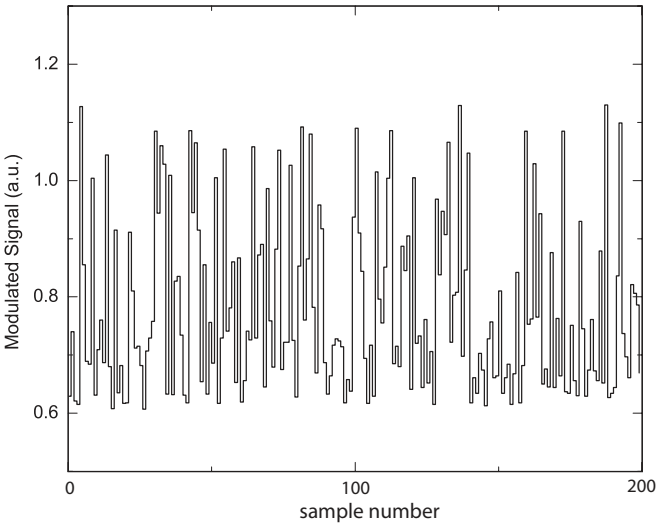

FIG. 3. SHG experimental data resulting from random field modulation. A transform-limited pulse was encoded as described in Eq. (23). The transform-limited phase produced a SHG signal ~ 1.1 corresponding to integration over an ultraviolet spectral window of 0.3 nm (equivalent to $\Delta\Omega = 2.8$ in pixel units) around the center of the spectrum at 398.3 nm. Shown are 200 randomly sampled data from the laboratory database of 1024 recorded points as explained in Sec. III. The vertical scale is proportional to the SHG signal and shows random variations around a mean level of $\sim$0.8. This dc level is due to the portion of the SHG signal not modified by the encoding. In the decoding operation 200,000 random samples were drawn from the recorded database to perform projections onto a hierarchy of decoding functions.

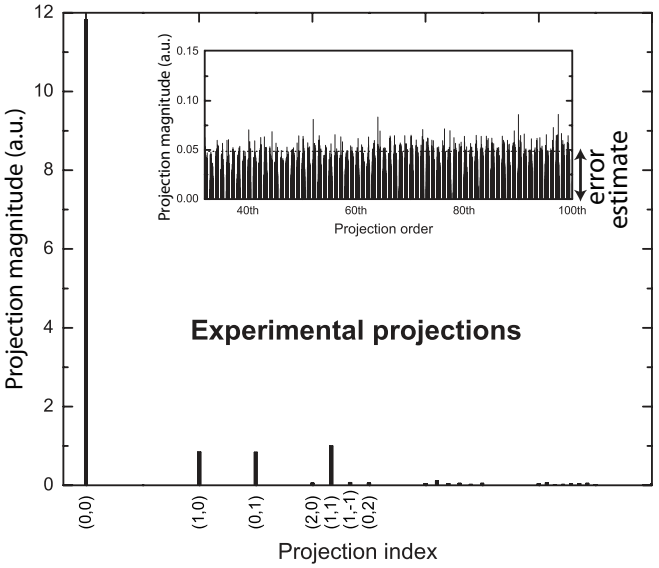

FIG. 4. Projections obtained from the experimental data with the projection indices being (j_1, j_2). Each projection has a (not shown here for clarity) corresponding c.c. projection of the same amplitude [i.e., projection (j_1, j_2) has a c.c. projection $(-j_1, -j_2)$]. The order of projection (j_1, j_2) is defined as $|j_1| + |j_2|$. High-order and very low value projections are not labeled in the main graph due to their close spacing. The inset zooms in at high-order projections (from the 32th to the 100th order) to show how the projection error was estimated as the mean value $\sim$0.05 of the high-order projections.

resolvable projection order as shown next. In the case of random-phase functions, a projection $P(j_1,j_2)$ is calculated from the modulated SHG signal as

$$P(j_1,j_2)=\frac{1}{N}\sum_{k=1}^{N}S_{\mathrm{SHG}}(s_k)\times e^{-i[j_1 f_1(s_k)+j_2 f_2(s_k)]}. \quad (24)$$

From the five-bit phase-resolution used here, the minimum phase difference between two contiguous points of the function $f_i(s_k)$ is equal to $\Delta\phi=2\pi/2^5=2\pi/32$. While this phase resolution is adequate to sample the functions $f_i(s_k),i=1$ and 2, high multiples of these functions will not be adequately sampled. For instance, the minimum phase difference between two contiguous points of the function $j_1 f_1(s_k)$ is $\Delta\phi_{j_1}=j_1\times 2\pi/32$. For $j_1\geqslant 32$, then $\Delta\phi_{j_1}\geqslant 2\pi$, and the function $j_1 f_1(s_k)$ (modulo 2π) will be distorted. Similarly the function $j_1 f_1(s_k)+j_2 f_2(s_k)$ is distorted for $|j_1|+|j_2|\geqslant 32$. As a result an observed nonlinear process corresponding to $|j_1|+|j_2|\geqslant 32$ would not be physically reliable, but in turn such an observed signal may be used as a basis to estimate the overall projection error. In the SHG illustration the projections are restricted to $|j_1|+|j_2|\leqslant 2$ on physical grounds (see Sec. V), and the resolution limit will not be reached. However, the resolution value of 32 permits an estimation of the combined effects of experimental noise and numerical error. The inset of Fig. 4 shows the magnitude of the high-order projections beyond 32, and their mean value is taken to establish the error level.

The errors in the projection ratios shown later in Table I were calculated from the projection errors using standard noise propagation formulas [i.e., the error $\pm\Delta r$ of the ratio $r=P_1/P_2$ can be obtained from the numerator and denominator errors ΔP_1 and ΔP_2 as $\Delta r/r=\pm\sqrt{(\Delta P_1/P_1)^2+(\Delta P_2/P_2)^2}$]. This formula is not accurate for very small value ratios, but it is still used here to estimate the error.

V. MECHANISM ANALYSIS OF THE SHG EXPERIMENTS

As explained earlier, the SHG system was chosen for its physical simplicity as an initial demonstration of HE-OD. The goal of the analysis in this section is to confirm the significant projection findings of Fig. 4 and to indicate how HE-OD projections can be interpreted.

Most of the field components were left unmodulated in the encoding described in Sec. IV B. Thus, Eq. (16) can be used here to interpret the experimental data directly from the projections of Fig. 4. As seen in the figure, there is a large decoded projection $P(0,0)$ corresponding to the high nominal dc level in the experimental signal (see Fig. 3). The highest-order projection over the resolution level is $P(1,1)$, indicating that the underlying physical process involved here is at most second order in the field. Also, the fact that $P(1,1)$ [and not $P(2,0)$ or $P(0,2)$] is present, indicates that cooperation among field components on opposite sides of the spectrum is important. There are also first-order projections $P(1,0)$ and $P(0,1)$, whose origin in the context of SHG will be explained in the following. Importantly, the logic of HE-OD does not require *a priori* knowledge of the system's Hamiltonian or its dynamics, as evident in Fig. 1 and the expression in Eqs. (12) or (16) corresponding to the decoded data. Each projection $P(j_1,\ldots,j_m)$ is a quantitative measure of the nonlinear interaction of the field components for their impact on the controlled dynamics. The HE-OD analysis of SHG will be performed first in a qualitative fashion followed by a quantitative comparison with numerical simulations.

For the qualitative analysis of the projection data, we simply treat the field amplitudes in the encoded spectral components on the left and the right of the spectrum as approximately constant and equal to E_1 and E_2, respectively (see Fig. 2). With this simplification the encoded field in Eq. (23) is now approximately given by

$$E^{\mathrm{enc}}(\omega,s_k)=\begin{cases}E_1\times e^{if_1(s_k)}, & \omega\sim(\omega_0-\omega_c),\\ E_2\times e^{if_2(s_k)}, & \omega\sim(\omega_0+\omega_c),\\ E(\omega), & \text{otherwise.}\end{cases} \quad (25)$$

Substituting the encoded field $E^{\mathrm{enc}}(\omega,s_k)$ of Eq. (25) for the field in the integrand of Eq. (21) gives the modulated SHG field at frequency $\Omega=2(\omega_0+\zeta)$, where ζ is a small shift from the center of the spectrum (see Fig. 2). When $\zeta=0$, all encoded spectral components multiply each other, producing only modulated terms of the form $e^{i[f_1(s_k)+f_2(s_k)]}$. On the other hand, when $\zeta\neq 0$ some encoded spectral components multiply nonencoded ones, resulting in the appearance of modulated terms of the form $e^{if_1(s_k)}$ and $e^{if_2(s_k)}$, as can be seen in Fig. 4. As ζ increases, the amplitude of the modulated term $e^{i[f_1(s_k)+f_2(s_k)]}$ decreases proportionately to ζ while the amplitude of the modulated terms $e^{if_1(s_k)}$ and $e^{if_2(s_k)}$ similarly increases. From these considerations and inspection of Fig. 2, the modulated SHG field is given by

$$E^{\mathrm{mod}}_{\mathrm{SHG}}(\Omega,s_k)\propto A'+B'(\zeta)e^{i[f_1(s_k)+f_2(s_k)]}+C'(\zeta)[e^{if_1(s_k)}+e^{if_2(s_k)}], \quad (26)$$

where

$$B'(\zeta)=(\Delta-2\zeta)E_1E_2, \quad (27)$$

$$C'(\zeta)=2\zeta E_1E_2, \quad (28)$$

and A' is the sum of all unmodulated pairs and is approximately a constant with respect to ζ, and $\Delta=5$ (in pixel units) is the width of the encoded regions of the spectrum. The quantities B' and C' are proportional to the small number of modulated pairs in Fig. 2, and thus the value of either of them is at most equal to $\sim\Delta E_1E_2$. There are $\Delta=5$ modulated pairs and $128/2-\Delta=59$ unmodulated pairs. Taking E_1E_2 as the approximate value of all pair products in Fig. 2, then we can estimate these parameters as $A'\sim 59E_1E_2$ and $B',C'\sim 5E_1E_2$, and we have

$$A'\gg B',C'. \quad (29)$$

Equation (29) is confirmed by the presence of a large dc component in the modulated signal (see Fig. 3.)

To calculate the observed modulated signal $S^{\mathrm{mod}}_{\mathrm{SHG}}(s_k)$ we integrate the squared modulus $|E_{\mathrm{SHG}}(\Omega,s_k)|^2$ over the measured frequency interval $\Delta\Omega$, as in Eq. (22). For a given SHG frequency $\Omega(\zeta)=2(\omega_0+\zeta)$, the measured "blue" (SHG) band $\Delta\Omega=2.8$ in the IR spectrum corresponds to

$\Delta\zeta$ =1.4 and hence to a half-bandwidth of $\zeta_m = 0.7$. With these parameters, the modulated signal is given by

$$\begin{aligned} S_{\mathrm{SHG}}^{\mathrm{mod}}(s_k) &\propto \int_{\Delta\Omega} \left|E_{\mathrm{SHG}}^{\mathrm{mod}}(\Omega,s_k)\right|^2 d\Omega \\ &\propto \int_{-\zeta_m}^{\zeta_m} \left|E_{\mathrm{SHG}}^{\mathrm{mod}}(\Omega(\zeta),s_k)\right|^2 d\zeta \\ &= 2\int_{0}^{\zeta_m} \left|E_{\mathrm{SHG}}^{\mathrm{mod}}(\Omega(\zeta),s_k)\right|^2 d\zeta \\ &\propto \{A + Be^{i[f_1(s_k)+f_2(s_k)]} + C[e^{if_1(s_k)} + e^{if_2(s_k)}] \\ &\quad + De^{i[f_1(s_k)-f_2(s_k)]} + c.c.\}, \end{aligned} \tag{30}$$

where

$$A = \int_0^{\zeta_m} |A'|^2 d\zeta \approx \zeta_m |A'|^2, \tag{31}$$

$$B = \int_0^{\zeta_m} A'^* B'(\zeta) d\zeta \approx A'^* \left(\Delta\zeta_m - \zeta_m^2\right) E_1 E_2, \tag{32}$$

$$C = \int_0^{\zeta_m} A'^* C'(\zeta) d\zeta \approx A'^* \zeta_m^2 E_1 E_2, \tag{33}$$

$$D = \int_0^{\zeta_m} B'(\zeta) C'^*(\zeta) d\zeta \approx 2\zeta_m^2 E_1^2 E_2^2. \tag{34}$$

Recall that $\Delta = 5$, $\zeta_m = 0.7$, and $A' \gg B', C' \sim E_1 E_2$. Since A is second order in A', while B and C are first order in A', and D is zeroth order in A', we have

$$A \gg B, \quad C \gg D.$$

Equation (30) shows how the original encoding of Eq. (23) affects the signal. The encoding produced terms linear in $\exp[if_1(s_k)]$ and $\exp[if_2(s_k)]$ as well as mixed bilinear terms $\exp\{i[f_1(s_k) + f_2(s_k)]\}$ and $\exp\{i[f_1(s_k) - f_2(s_k)]\}$ in the output signal. The modulated signal may be projected onto the set of functions $F(j_1, j_2; s_k) = \exp\{i[j_1 f_1(s_k) + j_2 f_2(s_k)]\}$ as explained in Sec. II to produce $P(j_1, j_2)$. From Eq. (30), the projections (as well as their c.c.) are $P(0,0) \approx A$, $P(1,1) \approx B$, $P(1,0) \approx C$, $P(0,1) \approx D$, and $P(1,-1) \approx D$. By using Eqs. (31)–(34) the projection ratios are predicted to satisfy the following relations:

$$\begin{aligned} \frac{P(0,0)}{P(1,1)} &\sim \frac{A}{B} \gg 1, \\ \frac{P(1,1)}{P(1,0)} &\sim \frac{B}{C} \approx \frac{\Delta - \zeta_m}{\zeta_m} > 1, \\ \frac{P(1,0)}{P(0,1)} &\sim \frac{C}{C} = 1, \\ \frac{P(1,-1)}{P(1,1)} &\sim \frac{D}{B} \ll 1. \end{aligned} \tag{35}$$

These results are in qualitative agreement with the laboratory projections of Fig. 4. No other projection has significant value over the estimated experimental noise level in Fig. 4. Also as expected, $P(1,-1)$ is very small and approximately lies at the noise level for these experiments.

For a more quantitative comparison with the experimental results, numerical simulations were carried out with the true form of the field, that is, $E(\omega)$ taken without the simplifying assumptions used earlier and with the inclusion of beam propagation effects. These effects are relevant since the coupling between the SHG and input laser beams can vary as both propagate through the nonlinear crystal due to imperfect phase matching. In our experiments the BBO crystal was critically phase matched by adjusting the angle of the crystal with respect to the input beam [28]. This results in near-perfect phase matching for spectral components close to the center of the spectrum, but the quality of the phase matching decreases for spectral components far from the center of the spectrum. This factor was taken into account in the numerical simulations since it can produce small effects but ones that are clearly observable with HE-OD.

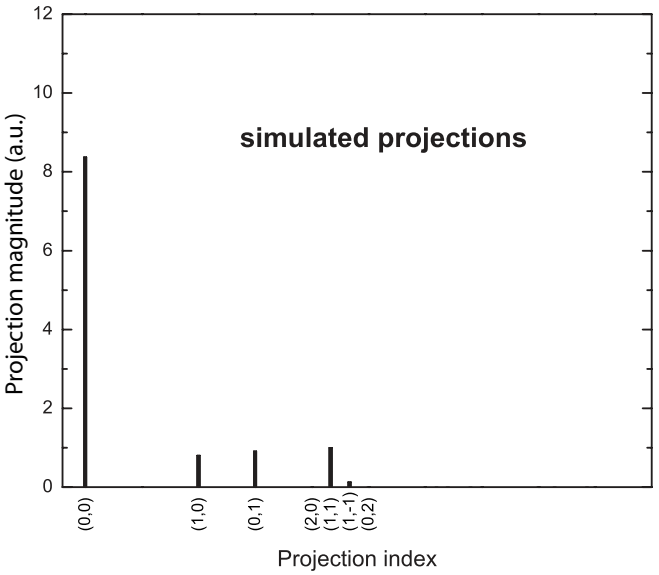

FIG. 5. Projections obtained from simulated data under similar conditions to those in the experiments.

The simulations were implemented in LabView using the LAB2 routine SFM CRYSTAL (nondepleted three-wave mixing) [33]. The input parameters were the same as for the experiment given in Sec. IV, including the crystal orientation set to $\phi = 0^\circ$ and $\theta = 29.178^\circ$ for angle phase matching. The LAB2 laser source that simulated the production of Gaussian pulses was set to high spectral resolution to allow for accurate modeling of the dynamics. The split-step method was used and dispersion effects of all orders were considered by using the Sellmeier equation to calculate the BBO crystal index of refraction. The results of these simulations are shown in Fig. 5.

A comparison between simulated and experimental projection ratios is given in Table I, where there is good quantitative

TABLE I. Comparison of simulated and experimental projection ratios. The experimental errors of the projection ratios were calculated from an error estimate in the data of 0.05 (obtained from the amplitude of the high-order projections as shown in the inset of Fig. 4) using standard error propagation formulas as indicated in Sec. IV B. $P(1,-1)$ was predicted to be small in Sec. V and its measured value lies near the experimental noise level.

	$P(1,1)/P(1,0)$	$P(1,0)/P(0,1)$	$P(1,-1)/P(1,1)$
Simulation	1.24	0.88	0.13
Experiment	1.19 ± 0.09	1.00 ± 0.08	0.06 ± 0.05

agreement. No ratio is shown involving projection $P(0,0)$ (a measure of the unmodulated portion of the signal), as the spectral data contained an arbitrary constant offset (i.e., the spectrometer signal was not zero for zero light intensity) that distorted the value of the experimental $P(0,0)$ value. The spectral offset does not affect the value of other projections, since a constant added to the signal does not affect the varying (ac) components. The projection $P(1,-1)$ should physically be present, but it should be small relative to the dominant terms $P(1,1)$, $P(0,1)$, and $P(1,0)$ as argued in Eq. (35). This behavior is confirmed in Fig. 4 where $P(1,-1)$ is at the noise level, and the observed ratio $P(1,-1)/P(1,1)$ is consistent with the simulations. Fig. 4 also shows a number of other small spurious projections at the noise level whose origin could be due to various experimental artifacts and the finite amount of data.

VI. CONCLUSIONS

The laboratory applicability of HE-OD was described in this work along with its successful illustration to the simple case of SHG to show the basic principles of the technique. HE-OD addresses the control mechanism by identifying the linear and nonlinear interactions between the field components in a chosen representation of the control, such as in Eq. (4). Any representation for the field can be employed with HE-OD, and, accordingly, the HE-OD mechanism assessment will reflect the choice of control field representation. This outcome is natural, as mechanism analysis of any form will be expressed with respect to some reference [11]. The only basic requirement is the ability to conveniently implement a particular field representation using a standard laboratory pulse shaper.

Any scheme aiming to extract quantitative information about the control mechanism requires knowledge of the laser field at the sample. This is particularly true for post-experiment modeling of dynamics that attempts to extract the mechanism from knowledge of the control field and the system Hamiltonian. In simple cases a calibration of the shaper will suffice to determine the field for an optically thin sample at weak field strengths. In the present illustration, detailed modeling (that included propagation effects) was used for comparison with the experimental findings of HE-OD, but that was not required here as the qualitative analysis of Sec. V demonstrated. In practice, HE-OD can always be performed to extract the projections $P(j_1,\ldots,j_m)$, but a full understanding of their physical meaning relies on an adequate knowledge of the field at the location of the test cell where the focal volume lies. Due attention needs to be paid to this issue, possibly including careful design of the test cell.

HE-OD can be adapted to any form of suitable experimental control data, including temporal observations. In this context, HE-OD may be viewed as a tailored sequence of encoded pump-probe experiments, where nonlinear relations between the controls (i.e., the pump) and the observations (i.e., the probe) are revealed in a hierarchical fashion. When $\rho(0)$ and $\hat{\mathcal{O}}$ are known, then HE-OD may be used to extract the physically relevant pathway amplitudes $U^{(n)}$ entering the expansion of U. In this sense HE-OD can be performed for quantum process tomography [34,35]. In turn, the correlations $P(j_1,j_2,\ldots,j_m)$ extracted from HE-OD data can be interpreted analogously to the correlations obtained by multidimensional (controlled) spectroscopy [36]. Importantly, HE-OD can be applied in cases where little information is available about the nature of the system's dynamics. In such circumstances, the decoded relationships between the field and the observations present insights into the detailed manipulation of the system that might, in turn, be used to aid in developing a model of the underlying dynamics. Furthermore, as indicated in Fig. 1, HE-OD may be included in closed-loop adaptive learning control to guide the search algorithm toward finding an optimal field that meets the control objective in balance with a desired mechanism.

ACKNOWLEDGMENTS

The authors would like to thank NSF, ARO, and Lockheed Martin for their support.

[1] R. S. Judson and H. Rabitz, Phys. Rev. Lett. **68**, 1500 (1992).
[2] C. Brif, R. Chakrabarti, and H. Rabitz (submitted to New J. Phys.).
[3] C. Daniel *et al.*, Chem. Phys. **267**, 247 (2001).
[4] M. Roth, L. Guyon, J. Roslund, V. Boutou, F. Courvoisier, J. P. Wolf, and H. Rabitz, Phys. Rev. Lett. **102**, 253001 (2009).
[5] T. Brixner and G. Gerber, Chem. Phys. Chem. **4**, 418 (2003).
[6] R. Bartels *et al.*, Nature (London) **406**, 164 (2000).
[7] T. Feurer, J. Vaughan, and K. Nelson, Science **299**, 374 (2003).
[8] M. Aeschlimann *et al.*, Nature (London) **446**, 301 (2007).
[9] T. Weinacht, J. Ahn, and P. Bucksbaum, Nature (London) **397**, 233 (1999).
[10] A. Mitra and H. Rabitz, Phys. Rev. A **67**, 033407 (2003).
[11] A. Mitra, I. R. Solá, and H. Rabitz, Phys. Rev. A **67**, 043409 (2003).
[12] A. Mitra and H. Rabitz, J. Phys. Chem. A **108**, 4778 (2004).
[13] A. Mitra and H. Rabitz, J. Chem. Phys. **125**, 194107 (2006).
[14] A. Mitra and H. Rabitz, J. Chem. Phys. **128**, 044112 (2008).
[15] K. Hoki and P. Brumer, Phys. Rev. Lett. **95**, 168305 (2005).
[16] C. Daniel *et al.*, Science **299**, 536 (2003).
[17] L. Pesce *et al.*, J. Chem. Phys. **114**, 1259 (2001).
[18] B. J. Pearson and P. H. Bucksbaum, Phys. Rev. Lett. **92**, 243003 (2004).
[19] T. Weinacht *et al.*, Chem. Phys. Lett. **344**, 333 (2001).
[20] F. Langhojer, D. Cardoza, M. Baertschy, and T. Weinacht, J. Chem. Phys. **122**, 014102 (2005).
[21] D. Cardoza, M. Baertschy, and T. Weinacht, J. Chem. Phys. **123**, 074315 (2005).
[22] D. Cardoza, M. Baertschy, and T. Weinacht, Chem. Phys. Lett. **411**, 311 (2005).
[23] D. Cardoza, C. Trallero-Herrero, F. Langhojer, H. Rabitz, and T. Weinacht, J. Chem. Phys. **122**, 124306 (2005).

[24] D. G. Kuroda, C. P. Singh, Z. Peng, and V. D. Kleiman, Science **326**, 263 (2009).
[25] G. Vogt, P. Nuernberger, R. Selle, F. Dimler, T. Brixner, and G. Gerber, Phys. Rev. A **74**, 033413 (2006).
[26] J. White, B. Pearson, and P. Bucksbaum, J. Phys. B **37**, L399 (2004).
[27] R. A. Bartels, M. M. Murnane, H. C. Kapteyn, I. Christov, and H. Rabitz, Phys. Rev. A **70**, 043404 (2004).
[28] R. Boyd, *Nonlinear Optics*, 2nd ed. (Academic Press, New York, 2003).
[29] T. Hornung, R. Meier, and M. Motzkus, Chem. Phys. Lett. **326**, 445 (2000).
[30] S. Fechner, F. Dimler, T. Brixner, G. Gerber, and D. Tannor, Opt. Exp. **15**, 15387 (2007).
[31] J. Vaughan, T. Feurer, K. Stone, and K. Nelson, Opt. Exp. **14**, 1314 (2006).
[32] B. J. Sussman, R. Lausten, and A. Stolow, Phys. Rev. A **77**, 043416 (2008).
[33] [http://www.physik.uni-jena.de/inst/lab2].
[34] J. Poyatos, J. Cirac, and P. Zoller, Phys. Rev. Lett. **78**, 390 (1997).
[35] M. Mohseni, A. T. Rezakhani, and D. A. Lidar, Phys. Rev. A **77**, 032322 (2008).
[36] D. Abramavicius and S. Mukamel, J. Chem. Phys. **120**, 8373 (2004).